

Weak bed control of the eastern shear margin of Thwaites Glacier, West Antarctica

Joseph A. MacGREGOR,¹ Ginny A. CATANIA,^{1,2} Howard CONWAY,³
Dustin M. SCHROEDER,¹ Ian JOUGHIN,⁴ Duncan A. YOUNG,¹ Scott D. KEMPF,¹
Donald D. BLANKENSHIP¹

¹*Institute for Geophysics, University of Texas at Austin, Austin, TX, USA*
E-mail: joemac@ig.utexas.edu

²*Department of Geological Sciences, University of Texas at Austin, Austin, TX, USA*

³*Department of Earth and Space Sciences, University of Washington, Seattle, WA, USA*

⁴*Polar Science Center, Applied Physics Laboratory, University of Washington, Seattle, WA, USA*

ABSTRACT. Recent acceleration and thinning of Thwaites Glacier, West Antarctica, motivates investigation of the controls upon, and stability of, its present ice-flow pattern. Its eastern shear margin separates Thwaites Glacier from slower-flowing ice and the southern tributaries of Pine Island Glacier. Troughs in Thwaites Glacier's bed topography bound nearly all of its tributaries, except along this eastern shear margin, which has no clear relationship with regional bed topography along most of its length. Here we use airborne ice-penetrating radar data from the Airborne Geophysical Survey of the Amundsen Sea Embayment, Antarctica (AGASEA) to investigate the nature of the bed across this margin. Radar data reveal slightly higher and rougher bed topography on the slower-flowing side of the margin, along with lower bed reflectivity. However, the change in bed reflectivity across the margin is partially explained by a change in bed roughness. From these observations, we infer that the position of the eastern shear margin is not strongly controlled by local bed topography or other bed properties. Given the potential for future increases in ice flux farther downstream, the eastern shear margin may be vulnerable to migration. However, there is no evidence that this margin is migrating presently, despite ongoing changes farther downstream.

INTRODUCTION

Thwaites Glacier drains part of the Amundsen Sea Embayment of the West Antarctic ice sheet. It is one of the largest and fastest-flowing glaciers in Antarctica and is presently losing mass at a rate that is surpassed only by the adjacent Pine Island Glacier (Shepherd and others, 2012). Recent changes on Thwaites Glacier include loss of ice-shelf buttressing (MacGregor and others, 2012a; Pritchard and others, 2012), rapid thinning (e.g. Pritchard and others, 2009) and acceleration across its grounding line (e.g. Rignot, 2008). Much of Thwaites Glacier is grounded well below sea level and its bed generally slopes downward heading inland (Holt and others, 2006), so it is potentially dynamically unstable if its grounding line retreats significantly (e.g. Schoof, 2007; Gudmundsson and others, 2012; Parizek and others, 2013). Understanding the dynamics of Thwaites Glacier and other overdeepened outlet glaciers in the Amundsen Sea Embayment is thus important for improving predictions of the contribution of the West Antarctic ice sheet to future sea-level rise (e.g. Joughin and Alley, 2011).

Although reported acceleration across Thwaites Glacier is currently confined to within ~40 km of the grounding line (Rignot, 2008), observations of thinning much farther upstream (Pritchard and others, 2012) raise questions about the potential vulnerability of its upstream ice-flow configuration to future changes (Parizek and others, 2013). Six distinct tributaries with speeds of $<100 \text{ m a}^{-1}$ in the glacier's drainage basin coalesce into its main trunk, which is up to 200 km wide. The shear margins that delineate the onset regions of these tributaries extend up to 300 km upstream of

the grounding line (Fig. 1). Surface speeds within the main trunk are non-uniform; in a central region up to ~40 km from the grounding line, surface speeds exceed 1 km a^{-1} . Slower ice flow ($100\text{--}500 \text{ m a}^{-1}$) outside this central region results in intraglacier zones with large lateral shear strain rates (up to 0.1 a^{-1} ; Lang and others, 2004; Fig. 1).

Bed topography and/or spatial variation in resistance to basal sliding largely determine the shear margin positions of many fast-moving glaciers and ice streams (Raymond and others, 2001). Resistance to basal sliding depends on several different subglacial properties, including basal hydrology, lithology and roughness (Winsborrow and others, 2010). Where abrupt changes in basal lubrication occur, shear margins may be inherently unstable due to thermomechanical feedbacks (Raymond, 1996; Jacobson and Raymond, 1998). Subglacial geology (e.g. the presence of deformable till) also influences the position of ice-stream margins (Anandakrishnan and others, 1998; Bell and others, 1998; Blankenship and others, 2001; Studinger and others, 2001). Most of Thwaites Glacier's tributaries clearly originate within bedrock troughs (Holt and others, 2006; Fig. 1), a pattern similar to that of the ice-stream tributaries in the Ross Sea Embayment (Joughin and others, 1999). The best example of this topographic control is the main trunk's western shear margin, which contours around several volcanoes/nunataks (including Mount Takahe and Mount Murphy) (Fig. 1). The role of bed topography is less clear along the eastern shear margin, as observed by Holt and others (2006) (Figs 1 and 2). At its upstream end, along the northern flank of the Byrd Subglacial Basin, the eastern shear margin roughly follows contours of bed elevation, but it is

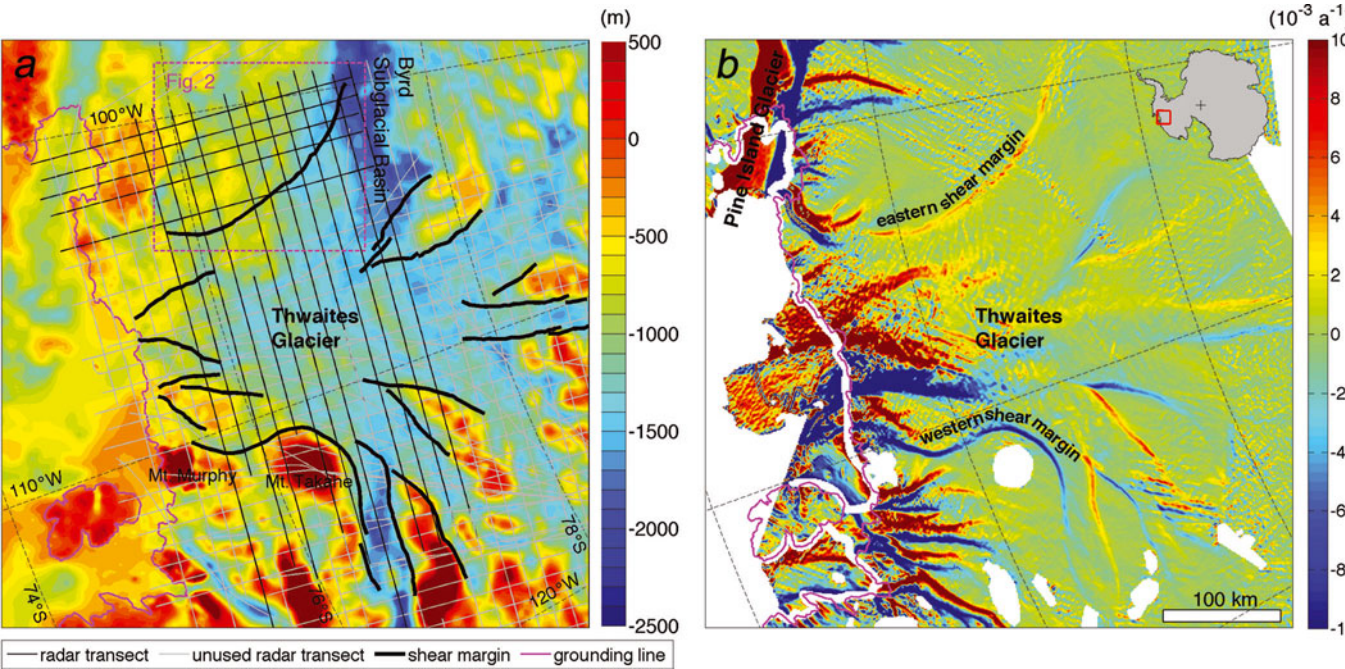


Fig. 1. (a) 1 km Bedmap2 bed elevation grid across Thwaites and Pine Island Glaciers (Fretwell and others, 2013; World Geodetic System 1984 (WGS84) ellipsoid). Contour interval 100 m. Manually traced shear margins, based on 1996 lateral shear strain rates shown in (b), are outlined by thick solid black lines. The grounding line is derived from the 2008–09 Moderate Resolution Imaging Spectroradiometer (MODIS) Mosaic of Antarctica (personal communication from T.A. Scambos and T. Haran, 2013). (b) Lateral shear strain rate ($\dot{\epsilon}_{xy}$; Eqn (A5) in Appendix). Positive (negative) values indicate right-handed (left-handed) shear, i.e. the along-flow surface velocity is decreasing to the right (left) of the flow direction. Inset map shows the location of the study area in Antarctica.

nearly perpendicular to those contours farther downstream. This pattern is not observed for any other of Thwaites Glacier’s tributary shear margins.

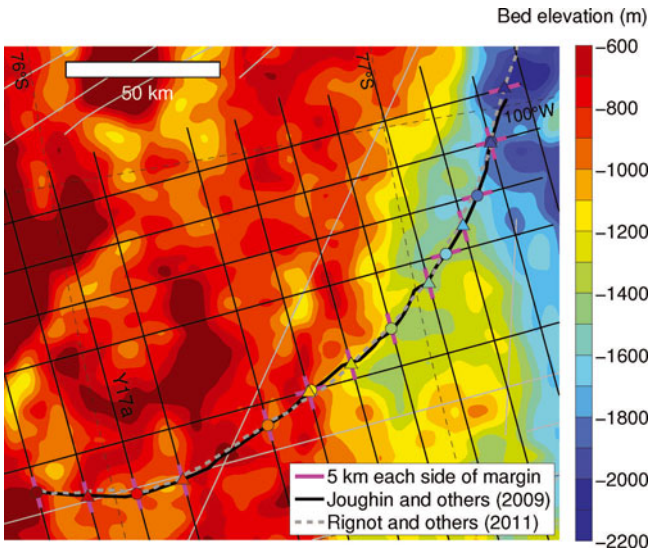


Fig. 2. Bedmap2 bed elevation in the vicinity of the eastern shear margin (Fretwell and others, 2013). The format is repeated from Figure 1a. Alternating colored circles and triangles mark the transect–margin intersections, which are used to distinguish these intersections in later figures. Table 1 lists the names of the Airborne Geophysical Survey of the Amundsen Sea Embayment, Antarctica (AGASEA) transects. Transects with low incidence angles ($<20^\circ$) relative to the shear margin are not included in this study. Also shown is the same shear margin traced using $\dot{\epsilon}_{xy}$ derived from the 2007–08 surface velocity field of Rignot and others (2011a), which is not substantially different from that derived using 1996 surface velocities.

To better understand the nature of the controls upon Thwaites Glacier’s eastern shear margin, in this study we investigate bed properties there using ice-penetrating radar data. Specifically, we use focused ice-penetrating radar transects to examine the topography and radar reflectivity of the bed. This approach is motivated by the variability in bed conditions across ice-stream shear margins reported by analogous studies of the Ross Sea Embayment. Downstream of their respective tributaries, the shear margins of the Ross ice streams are likely controlled by abrupt transitions in basal resistance to sliding (Raymond and others, 2001;

Table 1. AGASEA transects used in this study

Figure 3 label	Transect
a	X85a
b	X83a
c	Y35a
d	X81
e	Y33a
f	X79a
g	Y31b
h	Y29a
i	Y27a
j	X75a
k	Y25a
l	Y23a
m	Y19a
n	Y17a*
o	Y15b
p	Y13a

*Also shown in Figure 4.

Table 2. Values of static parameters in the radar equation (Eqn (1))

Symbol	Description	Value
P_t	Transmitted power	69 dBm
λ_{air}	Radar wavelength in air	5.0 m
G_a	Antenna gain	9.4 dB
T	Transmission loss at ice–air interface	−0.5 dB
	Total system loss	−4.0 dB
G_p	Processing gain	~68.5 dB
ϵ'_{ice}	Real part of the complex relative permittivity of pure ice	3.2

Catania and others, 2003), although the nature of this putative transition in the basal condition is poorly understood. For example, Peters and others (2005) found large (>10 dB) and abrupt (<5 km) decreases in bed reflectivity across portions of the downstream shear margins of Whillans and Kamb Ice Streams, which suggest that the bed there transitions abruptly from thawed beneath ice streams to frozen outside the margins. However, Raymond and others (2006) found no significant change in bed reflectivity across the same shear margin farther upstream on Whillans Ice Stream.

DATA

Surface velocity

We use surface velocity fields across Thwaites Glacier to locate the position of the eastern shear margin and to calculate lateral shear strain heating. Several glacier-wide maps of the 1996 surface velocity of Thwaites Glacier and adjacent glaciers have been produced using similar combinations of satellite-based synthetic aperture radar (SAR) interferometry and speckle tracking (Lang and others, 2004; Rignot and others, 2004; Joughin and others, 2009). Rignot and others (2011a) recently presented an Antarctic-wide surface velocity map, and the data in the coastal Amundsen Sea Embayment are mostly from 2007 and 2008. Because we focus on the eastern shear margin, which is farther upstream than the largest reported accelerations, and because we wish to maintain internal consistency with the temperature model later used to estimate englacial radar attenuation, here we use the 1996 surface velocity field presented by Joughin and others (2009).

We identify the position of the eastern shear margin by finding coherent maxima in the absolute value of the lateral shear strain rate field $\dot{\epsilon}_{xy}$ (Fig. 1), which is calculated from the gridded surface velocity field (Appendix). The width of the shear margins is typically <3 km and we estimate the uncertainty in our picks of $\dot{\epsilon}_{xy}$ maxima to be <1 km, based on the typical across-flow width of the peak in $\dot{\epsilon}_{xy}$. This width is similar to that observed for the Ross Sea ice streams, but measured strain rates there are significantly higher than for Thwaites Glacier (>0.07 a^{−1} for Whillans Ice Stream versus ~0.01 a^{−1} for Thwaites Glacier; e.g. Echelmeyer and others, 1994). This difference could be due to dynamical differences between these glaciers, the finer horizontal resolution of those field measurements compared with the 1 km grid spacing of the remotely sensed surface velocity field we used, or smoothing of the surface velocity field (Joughin and others, 2002).

Regional bed elevation

For a regional perspective of bed elevation across Thwaites Glacier (Figs 1a and 2), we use the 1 km resolution Bedmap2 bed elevation grid (Fretwell and others, 2013). In the vicinity of the eastern shear margin, this grid is derived mostly from the 60 MHz ice-penetrating radar transects collected by the Airborne Geophysical Survey of the Amundsen Sea Embayment, Antarctica (AGASEA) (Holt and others, 2006; Vaughan and others, 2006). Those AGASEA bed elevation data are based on bed picks made from unfocused SAR data, i.e. bed echoes that were coherently summed along-track without performing range migration.

Bed properties

The obfuscating effects of surface clutter and volume scattering from crevasses can be substantial across portions of Thwaites Glacier. To reduce these effects as much as possible and to improve along-track resolution, we study changes in radar-detected bed properties across the eastern shear margin using range-migrated SAR-focused airborne radar data collected by AGASEA. Peters and others (2005, 2007) summarized the radar system's characteristics and associated processing techniques. The bed was picked in the SAR-focused data using a semi-automatic algorithm that determines the location of the maximum bed echo intensity.

Bed reflectivity (R_b) is calculated using the radar equation (e.g. Peters and others, 2007):

$$P_r = P_t \left(\frac{\lambda_{\text{air}}}{4\pi} \right)^2 \frac{G_a^2 T^2 L_a^2 L_s G_p}{\left[2 \left(h + H / \sqrt{\epsilon'_{\text{ice}}} \right) \right]^2} R_b \quad (1)$$

where P_r is received power from the bed (bed echo intensity), P_t is the transmitted power, λ_{air} is the radar wavelength in air, G_a is the antenna gain, T is the transmission loss at the air–ice interface, L_a is the one-way loss due to dielectric attenuation, L_s is the total system loss, G_p is the processing gain, h is the height of the aircraft above the ice surface, H is the ice thickness and ϵ'_{ice} is the real part of the complex relative permittivity of ice. The values of the static system parameters in Eqn (1) are given by Peters and others (2007) and summarized here in Table 2.

Because of the challenge of calibrating inferred bed reflectivity values across regions of an ice sheet far inland from the grounding line, we instead consider the spreading- and attenuation-‘corrected’ bed echo intensity (P'_r), which is functionally identical to R_b in Eqn (1) and is also reported in decibels. We assume that P'_r does not necessarily represent the absolute reflectivity of the bed, but that its spatial variation does accurately capture the spatial variation of R_b . Implicit in this approach is the assumption that the unknown difference between P'_r and R_b did not change during the AGASEA survey and that this difference simply represents an unknown system calibration factor that is not presently included in Eqn (1).

For analyses of observed echo intensities using the radar equation (Eqn (1)), the most poorly constrained term is typically the loss due to dielectric attenuation (e.g. Peters and others, 2005, 2007; Matsuoka, 2011). Radio-frequency dielectric attenuation in polar ice depends primarily on temperature but also on impurity concentrations. To correct observed bed echo intensities for attenuation, we use the radar attenuation model presented by MacGregor and others (2007), which accounts for both temperature and chemistry.

Chemistry data are not yet available for the recently drilled deep ice core at the ice divide between the Ross and Amundsen Sea Embayments. The nearest deep ice core for which chemistry data are available is Siple Dome in the Ross Sea Embayment and here we assume that englacial impurity concentrations are uniform across our study area and are equal to the depth-averaged values at Siple Dome (MacGregor and others, 2007). The effect of the spatial variation of impurity concentrations should be small compared with that of englacial temperature (MacGregor and others, 2012b). Significant uncertainty remains in the parameterization of radar attenuation through ice (MacGregor and others, 2007), but here we ignore this uncertainty in our analysis because temperatures across the eastern shear margin likely vary smoothly and because we do not evaluate absolute values of bed reflectivity in terms of basal conditions.

To calculate temperature-dependent attenuation rates, we use a steady-state temperature model for Thwaites Glacier (Joughin and others, 2009). This model includes vertical diffusion of heat, horizontal and vertical advection of heat, vertical strain heating, and frictional heating at the bed. However, this temperature model does not include the effect of strain heating due to lateral shear and thus likely underestimates temperatures in the vicinity of the margins that are the focus of this study (Raymond, 1996; Harrison and others, 1998; Jacobson and Raymond, 1998; Raymond and others, 2001). To address this limitation, we estimate the temperature increase due to lateral shear strain heating (ΔT_{lat}) and treat it as a perturbation to the original model. First, we estimate the depth-averaged strain heating rate due to lateral shear ($\overline{W}_{\text{lat}}$) across Thwaites Glacier as

$$\overline{W}_{\text{lat}} = \frac{2\dot{\epsilon}_{xy}\overline{\tau}_{xy}}{\rho\bar{c}} \quad (2)$$

where $\overline{\tau}_{xy}$ is the depth-averaged lateral shear stress (Appendix), ρ is the density of pure ice (917 kg m^{-3}) and \bar{c} is the temperature-dependent depth-averaged specific heat capacity of pure ice, calculated following Cuffey and Paterson (2010, p. 400). Next, we determine the reversed horizontal particle paths p originating at each gridpoint (x, y) using the reversed surface velocity field $(-\vec{u}_s)$, and then calculate ΔT_{lat} during the period represented by the reversed particle path as

$$\Delta T_{\text{lat}}(x, y) = \int_{x_0, y_0}^{x, y} \frac{\overline{W}_{\text{lat}}(p(x, y))}{|\vec{u}_s(p(x, y))|} dp \quad (3)$$

where dp is the regular horizontal spacing of points along the particle path $p(x, y)$ and (x_0, y_0) is the upstream end of the particle path. This approach ignores diffusion of the additional heat generated by lateral shear (vertical diffusion is included in the original temperature model) and also assumes that ice flow was steady during the period taken for the particle to traverse its reversed path. Surface crevassing is not extensive across the eastern shear margin, so we ignore the effect that cold air pooling in crevasses has upon the near-surface thermal structure of the ice observed in more heavily crevassed margins (Harrison and others, 1998).

Based on surface velocities with a horizontal resolution of 1 km, $\overline{W}_{\text{lat}}$ is of the order of 10^{-3} K a^{-1} within the margins and up to 10^{-2} K a^{-1} within the intraglacier shear zones. The upper end of this range is similar to values inferred from borehole thermometry by Harrison and others (1998) for a

heavily crevassed margin of Whillans Ice Stream, although the horizontal resolution of their measurements was finer ($\sim 100\text{--}150 \text{ m}$) than that of the velocity grids used here. The total depth-averaged temperature perturbation is $<1 \text{ K}$ in the eastern shear margin, which is consistent with modeled patterns of heat generation at shear margins (Jacobson and Raymond, 1998). Without the temperature perturbation due to lateral shear strain heating, the mean difference between L_a on the fast and the slow sides of the eastern shear margin is $-0.6 \pm 1.9 \text{ dB}$. When this perturbation is included, the mean difference is $-0.3 \pm 2.0 \text{ dB}$. Although this correction is relatively small, we still include it in our attenuation model. Modeled attenuation rates increased from 13 to 18 dB km^{-1} between the upstream and downstream ends of the eastern shear margin.

MARGIN BED PROPERTIES

Bed elevation and reflectivity

All 16 radargrams that we examined are shown in Figure 3. An example transect is shown in more detail in Figure 4. The bed echo intensities derived from the radar data are much more variable along-transect compared with the relatively smooth bed topography. This variability is due to a combination of several factors: (1) bed roughness at scales comparable with the radar wavelength ($\lambda_{\text{ice}} = 2.8 \text{ m}$ for the 60 MHz data used here) (Grima and others, 2012); (2) clutter from the ice-sheet surface; (3) off-nadir signal; and (4) other noise in the focused data (Peters and others, 2007). To better distinguish across-margin differences in bed properties, we average values of bed elevation and bed echo intensity (uncorrected and corrected) across 5 km on either side of the margin (\overline{z}_b , \overline{P}_r and \overline{P}'_r , respectively). We then calculate the best-fit mean difference between the fast- and slow-flowing sides of the margin using a χ^2 minimization that accounts for the standard deviations of values on both sides of the margin. For bed elevation, this relationship is simply

$$\overline{z}_b^{\text{slow}} = \overline{z}_b^{\text{fast}} + \Delta z_b \quad (4)$$

where Δz_b is the best-fit mean difference between the bed elevation on the fast (inside) and slow (outside) sides of the margin for each transect; identical expressions are used to determine the best-fit values of ΔP_r and $\Delta \overline{P}'_r$. We chose a distance of 5 km on either side of the margin over which to average the data because this distance is 1.5–4.0 times the ice thickness across the eastern shear margin and should encompass its zone of thermodynamic influence (e.g. Echelmeyer and others, 1994; Jacobson and Raymond, 1998) and any transition in bed reflectivity (e.g. Catania and others, 2003). For Δz_b , we correct for the deviation of the transect–margin intersection from normal incidence, i.e. the apparent ‘dip’ of the bed. For ΔP_r and $\Delta \overline{P}'_r$, we averaged the data as linear power and converted back to decibels.

On the slower-flowing side of the eastern shear margin, bed elevations are higher for 11 of 16 transect–margin intersections, bed echo intensities are lower for 12 of 16 intersections, and bed reflectivities are lower for 11 of 16 intersections (Fig. 5). Because ice is generally thicker on the faster-flowing side, we might expect lower bed echo intensities on that side due to higher geometric spreading and attenuation losses if bed reflectivity was uniform across the margin (Eqn (1)). Instead, we observe the opposite pattern. After correcting for these losses, bed echo intensity

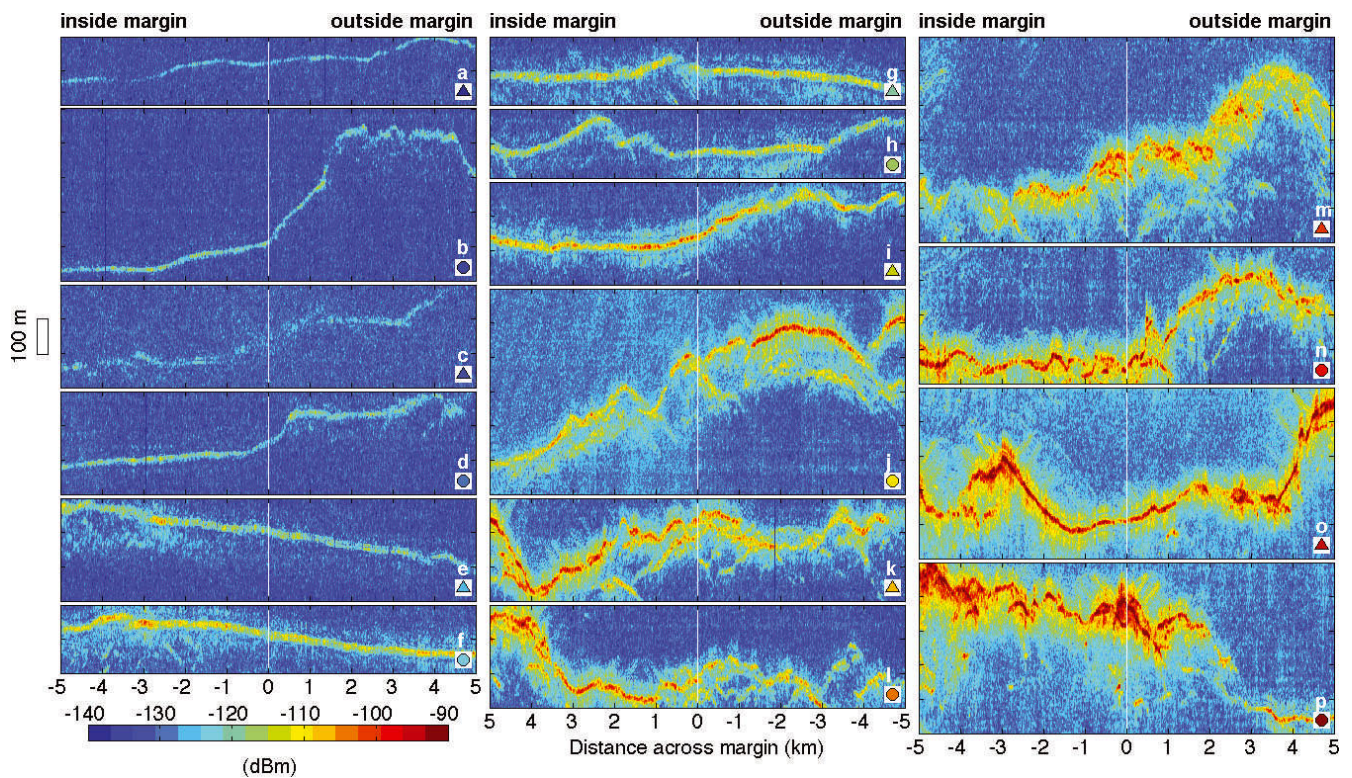


Fig. 3. Radargrams across all transect–margin intersections shown in Figure 2, shown from the upstream (top left) to downstream (bottom right) end of the eastern shear margin. The horizontal and vertical scales are the same for all radargrams. Symbols in the lower right corners of each panel follow Figure 2.

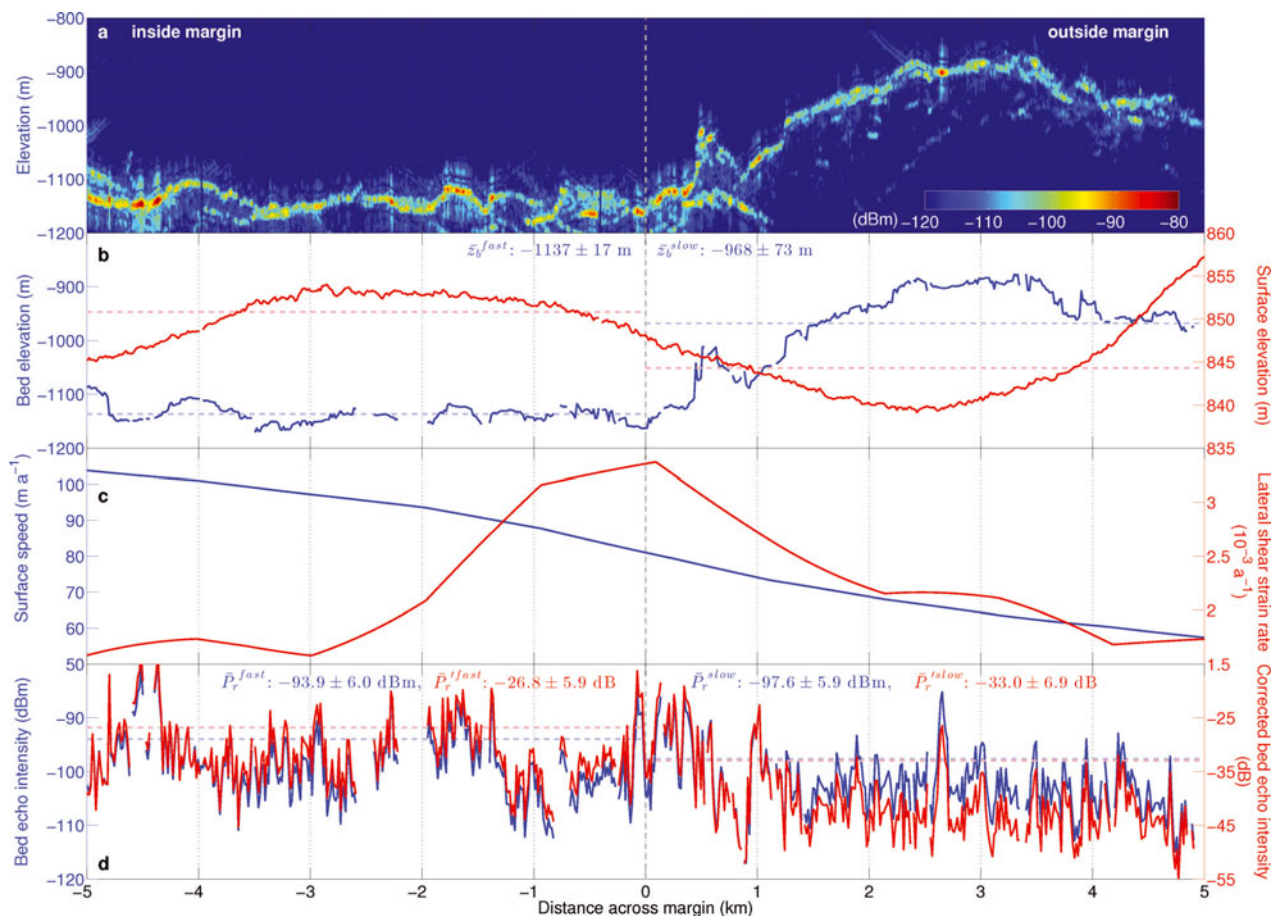


Fig. 4. (a) Example radargram across the eastern margin (transect Y17a; labeled in Fig. 2 and also shown in Fig. 3n). (b) Surface and bed elevation. (c) Surface speed and lateral shear strain rate. (d) Uncorrected and corrected bed echo intensity. Mean values of each property on either side of the margin are shown as horizontal dashed lines.

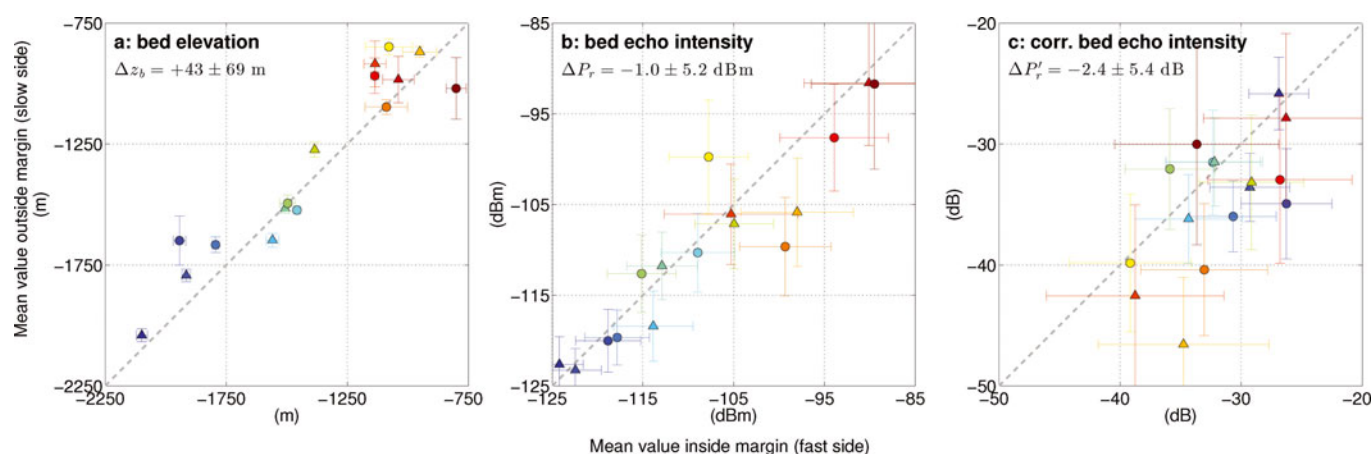


Fig. 5. (a) Mean bed elevation, (b) bed echo intensity and (c) corrected bed echo intensity for each transect 5 km on each side on the eastern shear margin. Each point represents a different transect–margin intersection, and their labeling follows Figure 2. Vertical (horizontal) error bars represent the standard deviation of each quantity on the slow (fast) side of the margin. Gray dashed lines represent 1 : 1 relationships between values on the fast and slow sides of the margin.

remains higher on the fast-moving sides of the margin (Figs 4d and 5c) and the across-margin difference in the attenuation correction due to lateral shear strain heating is too small to explain this difference.

The observed across-margin bed echo intensity differences are generally smaller than the predicted difference between frozen and unfrozen beds (10 dB or more; Peters and others, 2005). These smaller differences could be due to basal conditions that are more complex than simply frozen or thawed, suggesting a more complex subglacial environment that is qualitatively consistent with the predicted style of subglacial hydrology in ice-sheet interiors (e.g. distributed drainage; Carter and others, 2009). Alternatively, across-margin differences in bed roughness may cause the differences, which we consider in detail below.

Bed roughness

Topography

There are now several methods for quantifying bed roughness from bed topography, mostly using spectral methods to study macroscale (>500 m) bed roughness (e.g. Bingham and Siegert, 2009; Li and others, 2010; Rippin and others, 2011). Other methods examine the statistics of bed elevation and the bed echoes themselves (Rippin and others, 2006; Oswald and Gogineni, 2008). Collectively, these studies have considered a large range of roughness length scales (<1 m to 35 km) and found evidence of power-law relationships between roughness within this range of horizontal scales (e.g. Hubbard and others, 2000), implying a degree of self-affinity. Our focus on across-margin differences in bed properties precludes a straightforward comparison with the spectral roughness estimates from earlier studies because they investigated much larger horizontal scales of both roughness and variability in this larger-scale roughness. Furthermore, if the across-margin differences in bed echo intensity are due to roughness variations, then they will be most sensitive to roughness at scales close to the radar wavelength in ice (Ulaby and others, 1982). For a 60 MHz radio wave (wavelength in ice of 2.8 m), roughness at this scale cannot easily be measured directly by established spectral methods.

In its simplest form, bed roughness can be calculated as the standard deviation of the linearly detrended along-track

bed topography $z'_b(x)$ within a horizontal range of interest (Shepard and others, 2001). This form of bed roughness is the root-mean-square (rms) height ζ :

$$\zeta = \sqrt{\frac{1}{N-1} \sum_{i=1}^N [z'_b(x_i) - \bar{z}'_b]^2} \quad (5)$$

where \bar{z}'_b is the mean detrended bed elevation within the horizontal range of interest.

Bed roughness at a specified horizontal length scale Δx is calculated as the rms deviation ν of $z'_b(x)$ at intervals of Δx (e.g. Shepard and others, 2001):

$$\nu(\Delta x) = \sqrt{\frac{1}{N-1} \sum_{i=1}^N [z'_b(x_i) - z'_b(x_i + \Delta x)]^2} \quad (6)$$

The latter approach has also been used to study large-scale bed roughness of ice sheets (Young and others, 2011; Ross and others, 2012). Calculating the rms deviation for a range of horizontal length scales produces a bed roughness ‘spectrum’ analogous to that produced by spectral methods. An obvious lower limit for Δx is the mean horizontal posting of the focused radar data ($\Delta x_{\min} = 16.5$ m), which is an upper bound on the horizontal resolution of these data. A suitable upper limit is not as well constrained; Shepard and others (2001) suggested an upper limit to Δx equivalent to 10% of the length of the profile. For our analysis of 5 km on each side of the margin, this upper limit is 500 m. We calculate $\nu(\Delta x)$ across this range (16.5–500 m; Fig. 6) in order to later predict its value at smaller scales, because we are interested in the smaller-scale roughness that may influence bed reflectivity and/or basal drag. The roughness of natural surfaces is often self-affine across a wide range of length scales, i.e. roughness at one length scale often has a power-law relationship to roughness at another length scale (Shepard and others, 2001). For rms deviation, this relationship is expressed as

$$\nu(\Delta x) = \nu_0(\Delta x)^u \quad (7)$$

where ν_0 is the rms deviation at the horizontal unit scale (m), and u is the Hurst exponent, which is a measure of the self-affinity of a surface. The plausible range of u is $0 \leq u \leq 1$; as $u \rightarrow 1$, bump height approaches bump

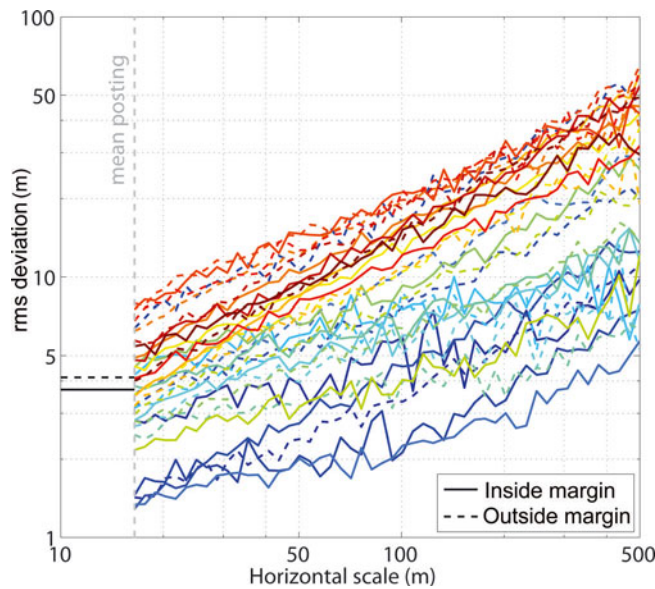


Fig. 6. Root-mean-square (rms) deviation of along-transect bed elevation vs horizontal length scale for each transect across the eastern shear margin, with colors following Figure 2. Vertical gray dashed line represents the mean posting between radar traces ($\Delta x_{\min} = 16.5$ m), i.e. the smallest horizontal scale for which rms deviation was calculated directly. Horizontal lines represent the mean values of rms deviation at the mean posting for the portions of the transect inside (solid lines) and outside (dashed lines) the margin.

wavelength at all length scales. We calculate the best-fit values of u and ν_0 for each side of each transect–margin intersection using linear regression in log space.

For the 32 rms deviation profiles shown in Figure 6 (one for each side of 16 transect–margin intersections), the mean Hurst exponent is 0.52 ± 0.15 . The mean difference between the measured and modeled values of $\nu(\Delta x_{\min})$ is $-1 \pm 8\%$ of the measured value and $1 \pm 22\%$ for $\nu(\Delta x = 500\text{ m})$. Of these profiles, 78% have data–model differences that are normally distributed, based on an a posteriori 95% confidence χ^2 test, and the mean p value of all data–model differences is 0.06 ± 0.15 . This good agreement across the range of horizontal length scales for which we calculated $\nu(\Delta x)$ suggests that bed elevation is indeed self-affine across this range. The mean rms deviation at the shortest measured length scale $\nu(\Delta x_{\min})$ is 3.7 ± 1.7 m on its fast side and 4.1 ± 1.9 m on its slow side (Fig. 6); these values are not significantly different ($p = 0.26$). Based on best-fit estimates of ν_0 (Eqn (7)), rms deviations at a horizontal scale of 1 m are both predicted to be on average 1 m on either side of the margin, i.e. they are indistinguishable given the ability of our method to resolve bed roughness at this scale. However, any physical interpretation of ν_0 assumes that the scale dependencies of the physical processes governing erosion, deposition and ultimately bed roughness at the scale of 1 m are unchanged between 1 m and Δx_{\min} .

Relationship with bed reflectivity

Because rough surfaces scatter reflected energy over a wider range of angles than smooth surfaces, the amplitude of nadir-reflected bed echoes decreases with increasing bed roughness (Ulaby and others, 1982). For unfocused radar-sounding data, most of the recorded energy is received from either nadir or near-nadir (within the first few Fresnel zones). The roughness-induced reflectivity decrease of a reflection

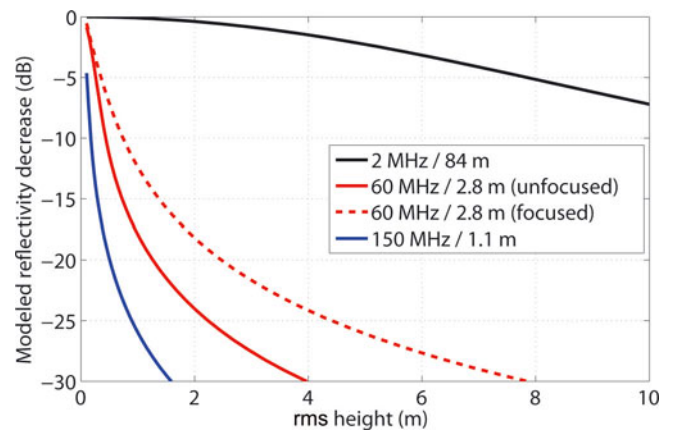


Fig. 7. Modeled reflectivity decrease due to roughness for three common ice-penetrating radar frequencies, including the center frequency of the radar data used in this study (60 MHz). Englacial wavelengths (λ_{ice}) for each center frequency are given in the legend. Solid lines represent the modeled reflectivity decrease at nadir for unfocused data (Eqn (8)). The rms height range is prescribed and similar to the observed range across the eastern shear margin. The dashed line is for the focused AGASEA data used in this study (Eqn (9)), assuming an aircraft altitude of 735 m, an ice thickness of 2461 m and a focusing window length of 2 km, which are typical values for the AGASEA data we evaluated. This modeled reflectivity decrease for focused data should not be considered valid for all SAR-focused radar surveys of ice sheets because ice thickness and survey design can vary significantly.

from nadir (ρ_n) can be modeled using Kirchhoff theory (Ogilvy, 1991) following Peters and others (2005) as

$$\rho_n = \exp(-g^2) I_0^2(g^2/2) \quad (8)$$

where $g = 4\pi\xi_{D_1}/\lambda_{\text{ice}}$ and I_0 is the zero-order modified Bessel function. The quantity g can be thought of as the wavelength-normalized rms height ξ_{D_1} . Peters and others (2005) describe this roughness metric (using the notation S) as ‘rms deviation’ (their eqn (8)). However, both their description of this quantity and a review of the origin of our Eqn (8) (Boithias, 1987) strongly suggest that rms height across a physically meaningful length scale should be used, not rms deviation at a specific horizontal scale. The subscript D_1 signifies that ξ_{D_1} is calculated across the width of the first Fresnel zone, the radius D_1 of which is calculated as

$$D_1 = \sqrt{2\lambda_{\text{ice}} \left(h + \frac{H}{\sqrt{\epsilon'_{\text{ice}}}} \right)} \quad (9)$$

For the 10 km long portions of the 16 transects that we studied, the mean value of D_1 is 134 ± 7 m.

Figure 7 shows the modeled effect of increasing roughness upon reflectivity based on Eqn (8) for several common ice-penetrating radar frequencies, including that used in this study. This relationship between unfocused radar reflectivity and roughness is consistent with several expectations: (1) reflectivity decreases with increasing roughness; (2) at a fixed bed roughness, the reflectivity decrease is smaller at larger englacial radar wavelengths (i.e. lower frequencies); and (3) where the bed is sufficiently rough, diffuse scattering begins to dominate the returned energy over that which is coherently reflected, so reflectivity does not decrease as rapidly.

Equation (8) considers only energy reflected from nadir, so it is not strictly applicable to the range-migrated focused data used in this study. This focusing uses matched filters to integrate received energy across a wider aperture ($\sim \pm 20^\circ$ from nadir) than a purely nadir return, so that energy reflected from a rough bed off-nadir but within the focusing aperture is included in the focused data. In other words, focusing partly corrects for the effect of bed roughness upon observed bed reflectivity. We next seek a relationship between bed reflectivity and roughness for focused radar data that satisfies three physically based assumptions: (1) any appropriate expression should approximate Eqn (8) for nadir-reflected energy within the first Fresnel zone; (2) off-nadir reflected energy is Gaussian-distributed and energy-conserving, following Nayar and others (1991); and (3) off-nadir energy in the along-track direction that is reflected within the range of angles spanned by the Doppler bandwidth of the focusing matched filter (i.e. its focusing aperture) is completely captured in the range-migrated focused data we used.

Following the above assumptions, this received energy can be modeled as the integral across the focusing aperture for a Gaussian function the width (effectively along-track length) of which is determined by the bed roughness. Increasing the width of the focusing aperture limits the decrease in along-track contribution to bed reflectivity due to increasing bed roughness. However, such mitigation is not possible in the across-track direction for the AGASEA radar system, because the bed is viewed from only one across-track look angle. The across-track contribution to bed reflectivity is therefore simply the integral of returned bed power across the first Fresnel zone (as for both the along-track and across-track directions in Eqn (7)) and is independent of the along-track focusing. The product of these two integrations (along-track and across-track) is the total effect of bed roughness upon its reflectivity. This product can be expressed compactly using the error functions that result from integrating Gaussian functions. For the mean aircraft survey height (735 m), ice thickness (2461 m) and focusing aperture of the range-migrated focused AGASEA radar-sounding data we used, the reduction in focused energy (ρ_f) as a function of bed roughness is

$$\rho_f = \operatorname{erf}\left(\frac{1.96}{g}\right) \operatorname{erf}\left(\frac{0.5}{g}\right) \quad (10)$$

where the first error function represents the integration of energy from the along-track focusing aperture and the second error function represents the integration of energy from the across-track angles spanned by the nadir-directed echo from the first Fresnel zone. As expected, Eqn (10) predicts a smaller reflectivity loss at any given roughness compared with Eqn (8) (Fig. 7).

Equation (10) predicts the reflectivity decrease due to roughness compared with a purely specular reflection, not the absolute bed reflectivity of the ice–bed interface. To evaluate these models, we compare $\Delta\rho_f$ (the difference between ρ_f values inside and outside the margin) to the observed differences in P'_r at the same locations (Fig. 8). These across-margin differences are independent of the absolute bed reflectivity R_b , but should be indicative of relative bed reflectivity differences and hence also corrected bed echo intensity differences ($\Delta\bar{P}'_r$). For the eastern margin, the correlation coefficient between the observed and modeled reflectivity differences is $r=0.67$. A unity correlation between the observed differences and $\Delta\rho_f$ would

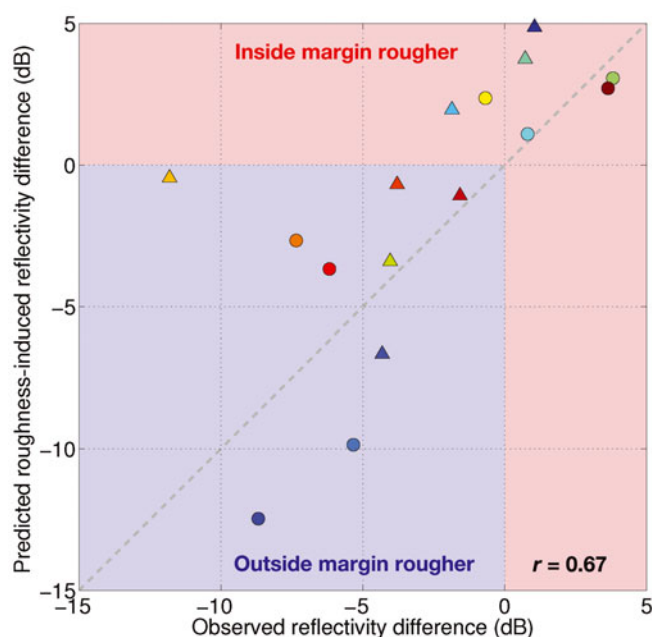


Fig. 8. Observed mean corrected bed echo intensity differences between inside and outside the margin vs the bed reflectivity differences predicted by Eqn (8), with labeling following Figure 2. Positive (negative) differences indicate that observed modeled reflectivity is higher outside (inside) the margin, implying the bed inside (outside) the margin is rougher. Gray dashed line represents a 1 : 1 relationship between the observed and predicted reflectivity differences.

imply that bed roughness completely controls the across-margin variability in P'_r . In general, Eqn (10) overestimates the observed reflectivity difference. This implies that, if all the observed reflectivity variability is due to roughness, then the focused radar data are less sensitive to bed roughness than Eqn (10) implies.

DISCUSSION

Nature of across-margin differences

Differences in bed elevation and reflectivity across the eastern shear margin suggest that both bed topography and some other property or combination of properties of the ice–bed interface influence the margin's position. The relationship with bed topography is not surprising, given the proportionality between ice thickness and driving stress. However, driving stress does not increase consistently across the eastern shear margin. Both sliding and deformation speeds are related nonlinearly to ice thickness. However, calculations using the temperature model applied above suggest that deformation speeds are $<10 \text{ m a}^{-1}$ across most of Thwaites Glacier. Thus, the increase in surface velocity across the eastern shear margin (e.g. a doubling in speed along transect Y17a in the vicinity of the eastern shear margin; Fig. 4c) is unlikely to be due to changes in deformation speed. Anandakrishnan and others (1998) made a similar argument to support their inference (from seismic data) that changes in subglacial geology affect ice flow across the margin of Whillans Ice Stream.

The broadly negative correlation between bed elevation and reflectivity across the eastern shear margin implies that either the dielectric contrast of the ice–bed interface, its

roughness or a combination of these two properties changes there. At 60 MHz, a bed reflectivity change of ~ 5 dB beneath grounded ice suggests a change between unfrozen till and unfrozen bedrock, while a change of >10 dB suggests a change between a frozen and unfrozen bed, whether till or bedrock (Peters and others, 2005). We observed bed reflectivity differences both below and above 10 dB, implying that both transitions are present, but there was no clear along-transect pattern (Fig. 5c). On average, these differences are <5 dB, which suggests that the change in the nature of the bed is generally lithological or morphological, rather than thermal. The importance of an unfrozen bed that has a pressurized subglacial hydrological system for inducing significant basal sliding is well established, while the role of bed roughness and smaller changes in lithology is less clear (Cuffey and Paterson, 2010).

A possible change in lithology may be related to the change in bed elevation. Virtually all of Thwaites Glacier is grounded well below sea level (Holt and others, 2006; Fig. 1). During interglacial periods when Thwaites Glacier was thinner than at present, areas outside its margins would have remained grounded longer because they are generally higher. Thus, we might expect thinner layers of potentially deformable marine sediment deposited outside the margins (or even their absence), as has been suggested for the Ross Sea ice streams (Joughin and others, 1999). However, the small mean difference in bed elevation across the eastern shear margin (43 ± 69 m) suggests that any lithological change across this margin due to this hypothesized spatial variability in depositional environment is unlikely to be significant.

We next consider the possible role of changes in bed roughness in modulating the position of the eastern shear margin, as our analysis suggests that bed roughness changes can explain much of the change in bed reflectivity observed there. Rippin and others (2011) examined bed roughness at horizontal scales of several hundreds of meters across Pine Island Glacier using spectral methods. They found that ice-flow speed and bed roughness were inversely related on regional scales, and a rougher bed outside at least one tributary. However, they also found smooth beds in some inland areas of slow ice flow. Based on those observations, they argued for an indirect relationship between bed roughness and ice-flow speed. They suggested that smooth beds do not necessarily increase rates of basal sliding, but rather that they lower the basal drag that mostly balances the driving stress. Our results are consistent with their observations and can be used to refine their hypothesis because we focus on bed roughness across large transitions in ice dynamics and we resolve finer scales (down to 16.5 m) of bed roughness that are much closer to the controlling obstacle size that most strongly affects basal drag (<1 m; e.g. Cuffey and Paterson, 2010).

In general, faster-flowing ice overlies smoother beds, but this relationship is apparently nonlinear, as suggested by Rippin and others (2011) and predicted by theory (e.g. Cuffey and Paterson, 2010, p. 229–238). For the radar transect that crosses the eastern shear margin shown in Figure 4, the surface speed approximately doubles across the margin. Because both sides of the margin are believed to be flowing mostly by basal sliding (based on model estimates of deformation speed), the speed difference probably does not indicate the onset of basal sliding, but rather a change in its magnitude. While bed roughness and reflectivity are overall related across the eastern shear margin, we did not observe

significant differences in bed roughness at the shortest resolvable length scales. Using the same radar data as this study, Schroeder and others (in press) also did not observe any clear change in the specularity of bed echoes across the eastern shear margin, further suggesting that bed roughness did not change significantly there. These results emphasize the limitations of our approach to resolving bed roughness and our understanding of its relationship to ice flow, particularly for the soft bed that is likely present along the eastern shear margin.

The magnitude of lateral drag peaks in the vicinity of margins and it reduces the basal drag required to balance the driving stress locally inside the margin. Given their relationship with margin position, the variability in bed roughness we observed is a plausible but not yet definitive mechanism for explaining the expected change in basal drag. Changes in subglacial hydrology or some other bed property (e.g. till rheology) are also plausible and the occasionally large bed reflectivity changes we observed (>10 dB; Fig. 5c) suggest that hydrologic transitions may also be present along short portions of the margin. However, bed roughness provides the most consistent explanation for the across-margin difference in bed reflectivity at the scale we considered.

The basal drag modelling results of Joughin and others (2009) do not extend beyond Thwaites Glacier's outermost shear margins, so we cannot discuss our across-margin observations in terms of existing predictions of the spatial variation of basal drag. Within the glacier, Joughin and others (2009) observed several regions of high basal drag oriented across-flow and separated by regions of very low basal drag. This pattern implies the presence of both hard bedrock and weak till underneath Thwaites Glacier and frames an important question regarding the bed roughness variability we observed: is it a control on, or a consequence of, ice flow? Theoretical studies of the relationship between bed roughness and basal drag are often predicated upon the notion that the bed is hard, but that is unlikely to be the case here. Additional field observations and models are necessary to resolve the relationship between bed roughness and basal drag for soft beds, as also suggested by Rippin and others (2011). Other West Antarctic glaciers can mobilize basal sediment on decadal timescales (Smith and others, 2007, 2012), so it is certainly plausible that Thwaites Glacier has also eroded its bed differentially in a manner that altered basal drag since the last collapse of the West Antarctic ice sheet ~ 200 ka ago (Pollard and DeConto, 2009). We hypothesize that the bed roughness variability we observed is a consequence of ice flow as sediment is remobilized.

Our results also hint at a possible explanation for the perplexing result reported by Raymond and others (2006), who observed no change in bed reflectivity across the 'Snake' shear margin of Whillans Ice Stream using 2 MHz ice-penetrating radar. Figure 7 shows that 2 MHz radar is not sensitive to bed roughness at vertical scales of <10 m. For Thwaites Glacier, observed rms deviation at a horizontal scale of 85 m (the wavelength of 2 MHz radar in ice) across the eastern shear margin is ~ 5 m, although it varies between 2 and 20 m (Fig. 6). At 2 MHz, an rms deviation of 5 m would produce a relatively small reflectivity decrease of ~ 3 dB in bed reflection power (Fig. 7). If the spatial variation of bed roughness across the Snake is similar to, or lower than, that of Thwaites Glacier's eastern shear margin, then it is plausible that this roughness pattern could be present without having been detected by 2 MHz radar. Whether this

pattern modulates ice flow there or vice versa would be subject to the same uncertainties as described above for Thwaites Glacier's eastern shear margin.

Implications for margin stability

In part due to their internal dynamics, the Ross Sea ice streams migrate and undergo changes in flow speed (e.g. Hulbe and Fahnestock, 2007; Catania and others, 2012). Comparatively little is known regarding the long-term flow history of Thwaites Glacier, although its modern thinning rates are an order of magnitude faster than those of adjacent glaciers averaged over the last 4.7–14.5 ka (Johnson and others, 2008). This limited understanding of the long-term flow history of Thwaites Glacier motivates evaluation of its present ice-flow configuration.

Given the across-margin differences we observed and the limited bed controls that they imply, we can make some inferences regarding the stability of Thwaites Glacier's eastern shear margin. This margin is slightly higher, dimmer (in terms of radar reflectivity) and rougher on its slow side (Figs 5 and 6). This pattern suggests one of two scenarios: (1) the modest across-margin differences in bed properties are sufficient to change the basal drag and hence the driving stress, producing a distinct shear margin; or (2) the edge of the Byrd Subglacial Basin, where the margin's trace is more clearly normal to the regional bed slope (Fig. 2), is sufficient to initiate the eastern shear margin and maintain a dynamical configuration at odds with the regional bed topography farther downstream, which otherwise suggests a more westerly path. Rippin and others (2011) found that Byrd Subglacial Basin is relatively smooth at horizontal scales of several hundred meters, but that a rougher bed exists eastward of that basin, including the area crossed by the eastern shear margin. Given the self-affinity of bed roughness (e.g. Fig. 6), their results also seem to suggest a more westerly path for the eastern shear margin. The first scenario (across-margin differences alone produce the margin) would seem to be less stable, because thickness changes across Pine Island and Thwaites Glaciers would likely alter the local force balance more quickly, but we cannot yet determine which is correct.

A qualitative investigation of the internal stratigraphy in the vicinity of the eastern shear margin found the expected dominant pattern, i.e. the internal stratigraphy is smooth and draped over the bed topography (Karlsson and others, 2009). Similarly, we observed no clear change in the internal stratigraphy across the eastern shear margin, nor did we observe any features that suggested recent or longer-term migration of its position. However, we did not trace the internal stratigraphy in detail in this study, which could provide more quantitative insight into the strain history of the ice sheet in this region. Firmer conclusions regarding the strain history there must therefore await further research.

The maximum difference between the position of the eastern shear margin derived from the 1996 and 2007–08 surface velocity datasets is ~ 1 km (Joughin and others, 2009; Rignot and others, 2011a), with no clear trend of inward or outward migration (Fig. 2). If we treat that maximum difference as a real migration, then the maximum margin migration rate over this ~ 12 year period is $<0.1 \text{ km a}^{-1}$. This value is within the range of migration rates reported for portions of Whillans Ice Stream (Harrison and others, 1998; Stearns and others, 2005), but that ice stream is likely much more vulnerable to margin migration than Thwaites Glacier

due to the former's dynamical configuration (i.e. margin-controlled force balance; Raymond and others, 2001). Given that the 1996 and 2007–08 surface velocity fields are gridded at 1.0 and 0.9 km, respectively, the null hypothesis that the eastern shear margin remained stable during this period cannot be invalidated. The small observed differences are likely either gridding artifacts, noise in the surface velocity fields or errors in our margin tracing.

Finally, we note that the downstream end of Thwaites Glacier's eastern shear margin is <50 km from the onset of an unnamed outlet glacier between Thwaites and Pine Island Glaciers (Fig. 9). This glacier was labeled 'SW tributary' by MacGregor and others (2012a), although in the strictest sense it is not a tributary of Pine Island Glacier but rather of its ice shelf. Since late 2001, the southern shear margin of Pine Island Glacier's ice shelf has retreated progressively by ~ 5 km and rifts have grown along this shear margin (MacGregor and others, 2012a). This glacier is also presently thinning (Pritchard and others, 2012), which is likely due to its recent acceleration (Rignot, 2008) and connected to increased sub-ice-shelf melting in the eastern Amundsen Sea Embayment (Jacobs and others, 2011). If this ice-shelf rifting and retreat evolves in the coming decades in a manner similar to that of the more dramatic rifting and retreat of this ice shelf's northern shear margin (a 21 km long rifted zone has developed and disintegrated there over the same period) and other outlet glaciers in this region, then this glacier will eventually lose whatever buttressing is currently provided by Pine Island Glacier's ice shelf (MacGregor and others, 2012a).

An increase in grounding-line ice flux due to buttressing loss can alter ice dynamics far upstream of the grounding line (e.g. Scambos and others, 2004; Scott and others, 2009). Given the weak bed control of the eastern shear margin that we inferred from radar observations, we speculate that the eastern shear margin would migrate outward in response to a substantially increased ice flux, expanding the fast-flow region of Thwaites Glacier. This ice-flux change could originate from the 'SW tributary' as described above or the mass loss of Thwaites Glacier proper (its main trunk) could continue and induce such a change. However, as described above, the eastern shear margin has not clearly migrated during a period contemporaneous with these changes.

CONCLUSIONS

We found that the dynamic transition between Thwaites and Pine Island Glaciers represented by Thwaites Glacier's eastern shear margin is coincident with modest radar-observed changes in bed properties there. While the bed topography is generally higher, these differences do not appear to be sufficient to explain the change in ice dynamics. Bed roughness variability can explain the observed bed reflectivity change and is consistent with the pattern of ice flow, but not significantly so. It remains unclear whether this pattern is a result of or a modulator of increased basal sliding, but the likely presence of marine sediment along the length of the margin implies the former.

That we observed little change in the nature of the bed across the eastern shear margin is interesting, especially given its ambiguous relationship with regional bed topography. We did not investigate in detail the bed of the ~ 100 km wide region between Thwaites and Pine Island Glaciers' tributaries, although we note that its elevation is

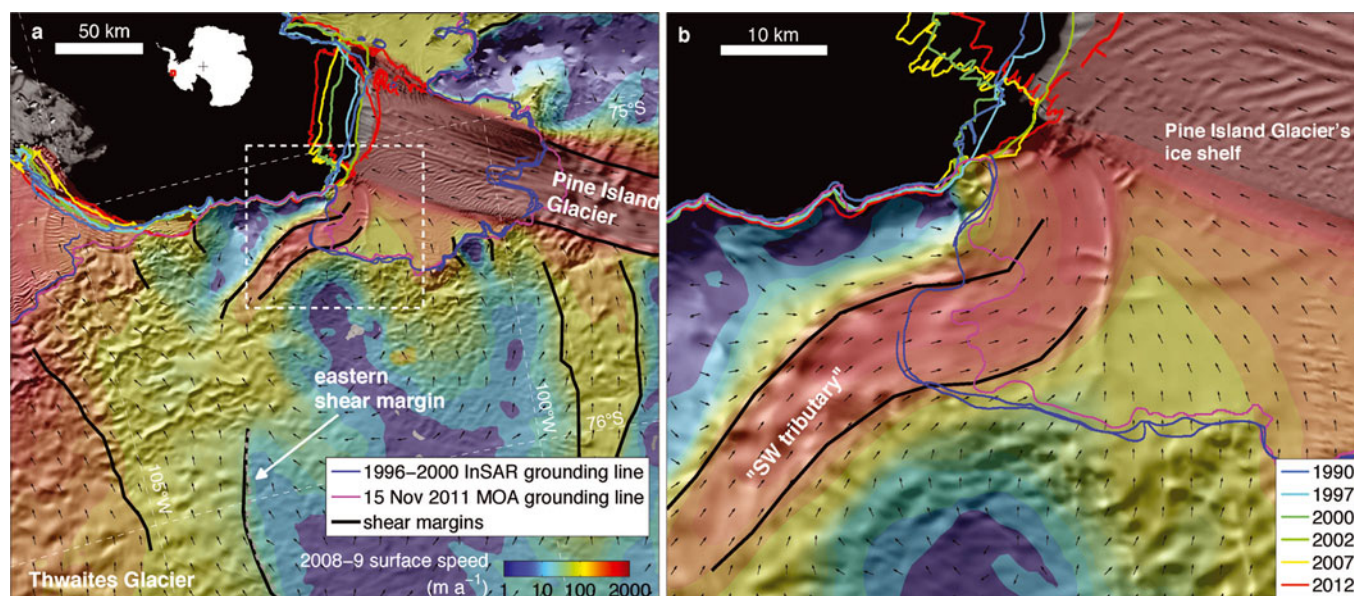


Fig. 9. (a) Surface velocity (Rignot and others, 2011a) and recent coastline history (MacGregor and others, 2012a) of Thwaites and Pine Island Glaciers in the vicinity of the downstream end of the eastern shear margin. Background image is the 2008–09 MODIS Mosaic of Antarctica (MOA) and the MOA grounding line is derived from this image (personal communication from T.A. Scambos and T.M. Haran, 2013). The interferometric SAR (InSAR)-derived grounding line is from Rignot and others (2011b). (b) Expanded view in the vicinity of the southern shear margin of Pine Island Glacier's ice shelf. The legend gives years of traced coastlines from MacGregor and others (2012a), except for the 2012 coastline, which was traced using the same methodology described therein.

generally several hundred meters higher than that at the eastern shear margin and that it is even higher across a dome-shaped rise between two southern tributaries of Pine Island Glacier (Fig. 1). Furthermore, Rippin and others (2011) found that the bed in this inter-tributary region was rough at larger horizontal scales. Thus, the eastern shear margin may have limited potential to migrate outwards beyond the narrow region we investigated here. There is no evidence of significant margin migration during the most recent two decades, a period during which acceleration and major coastal changes for both Thwaites and Pine Island Glaciers were observed. However, the potential for future increases in ice flux farther downstream indicates that the position of this shear margin should continue to be monitored.

AUTHOR CONTRIBUTION STATEMENT

J.A.M., G.A.C., H.C. and D.D.B. designed this study. D.M.S. developed the relationship between bed roughness and radar reflectivity. I.J. provided the temperature model and 1996 surface velocity data. D.A.Y, S.D.K and D.D.B. collected and processed the radar data. J.A.M. performed the analysis and wrote the manuscript. All authors discussed the results and edited the manuscript.

ACKNOWLEDGEMENTS

The US National Science Foundation (ANT 0424589, 0739654 and 0739372) supported this work. We thank S.F. Price, T.J. Fudge and T.A. Scambos for valuable discussions, and S.C. Rybarski and S.K. Young for tracing the 2012 coastline of the eastern Amundsen Sea Embayment. We thank the scientific editor (N. Glasser), R. Drews and an anonymous reviewer for constructive comments that improved the manuscript.

REFERENCES

- Anandakrishnan S, Blankenship DD, Alley RB and Stoffa PL (1998) Influence of subglacial geology on the position of a West Antarctic ice stream from seismic observations. *Nature*, **394**(6688), 62–65 (doi: 10.1038/27889)
- Bell RE and 6 others (1998) Influence of subglacial geology on the onset of a West Antarctic ice stream from aerogeophysical observations. *Nature*, **394**(6688), 58–62 (doi: 10.1038/27883)
- Bingham RG and Siegert MJ (2009) Quantifying subglacial bed roughness in Antarctica: implications for ice-sheet dynamics and history. *Quat. Sci. Rev.*, **28**(3–4), 223–236 (doi:10.1016/j.quascirev.2008.10.014)
- Blankenship DD and 9 others (2001) Geologic controls on the initiation of rapid basal motion for West Antarctic ice streams: a geophysical perspective including new airborne radar sounding and laser altimetry results. In *The West Antarctic ice sheet: behavior and environment*. (Antarctic Research Series 77) American Geophysical Union, Washington, DC, 105–121
- Boithias L (1987) *Radiowave propagation*. McGraw-Hill, New York
- Carter SP, Blankenship DD, Young DA, Peters ME, Holt JW and Siegert MJ (2009) Dynamic distributed drainage implied by the flow evolution of the 1996–1998 Adventure Trench subglacial lake discharge. *Earth Planet. Sci. Lett.*, **283**(1–4), 24–37 (doi: 10.1016/j.epsl.2009.03.019)
- Catania GA, Conway H, Gades AM, Raymond CF and Engelhardt H (2003) Bed reflectivity beneath inactive ice streams in West Antarctica. *Ann. Glaciol.*, **36**, 287–291
- Catania GA, Scambos TA, Conway H and Raymond CF (2006) Sequential stagnation of Kamb Ice Stream, West Antarctica. *Geophys. Res. Lett.*, **33**(14), L14502 (doi: 10.1029/2006GL026430)
- Catania G, Hulbe C, Conway H, Scambos TA and Raymond CF (2012) Variability in the mass flux of the Ross ice streams, West Antarctica, over the last millennium. *J. Glaciol.*, **58**(210), 741–752 (doi: 10.3189/2012JoG11J219)
- Cuffey KM and Paterson WSB (2010) *The physics of glaciers*, 4th edn. Butterworth-Heinemann, Oxford
- Echelmeyer KA, Harrison WD, Larsen C and Mitchell JE (1994) The role of the margins in the dynamics of an active ice stream. *J. Glaciol.*, **40**(136), 527–538

- Fretwell P and 55 others (2013) Bedmap2: improved ice bed, surface and thickness datasets for Antarctica. *Cryosphere*, **7**(1), 375–393 (doi: 10.5194/tc-7-375-2013)
- Grima C, Kofman W, Herique A, Orosei R and Seu R (2012) Quantitative analysis of Mars surface radar reflectivity at 20 MHz. *Icarus*, **220**(1), 84–99 (doi: 10.1016/j.icarus.2012.04.017)
- Gudmundsson GH, Krug J, Durand G, Favier L and Gagliardini O (2012) The stability of grounding lines on retrograde slopes. *Cryosphere*, **6**(6), 1497–1505 (doi: 10.5194/tc-6-1497-2012)
- Harrison WD, Echelmeyer KA and Larsen CF (1998) Measurement of temperature in a margin of Ice Stream B, Antarctica: implications for margin migration and lateral drag. *J. Glaciol.*, **44**(148), 615–624
- Holt JW and 8 others (2006) New boundary conditions for the West Antarctic ice sheet: subglacial topography of the Thwaites and Smith glacier catchments. *Geophys. Res. Lett.*, **33**(9), L09502 (doi: 10.1029/2005GL025561)
- Hubbard B, Siegert MJ and McCarroll D (2000) Spectral roughness of glaciated bedrock geomorphic surfaces: implications for glacier sliding. *J. Geophys. Res.*, **105**(B9), 21 295–21 303 (doi: 10.1029/2000JB900162)
- Hulbe C and Fahnestock M (2007) Century-scale discharge stagnation and reactivation of the Ross ice streams, West Antarctica. *J. Geophys. Res.*, **112**(F3), F03S27 (doi: 10.1029/2006JF000603)
- Jacobs SS, Jenkins A, Giulivi CF and Dutrieux P (2011) Stronger ocean circulation and increased melting under Pine Island Glacier ice shelf. *Nature Geosci.*, **4**(8), 519–523 (doi: 10.1038/ngeo1188)
- Jacobson HP and Raymond CF (1998) Thermal effects on the location of ice stream margins. *J. Geophys. Res.*, **103**(B6), 12 111–12 122 (doi: 10.1029/98JB00574)
- Johnson JS, Bentley MJ and Gohl K (2008) First exposure ages from the Amundsen Sea Embayment, West Antarctica: the Late Quaternary context for recent thinning of Pine Island, Smith and Pope Glaciers. *Geology*, **36**(3), 223–226 (doi: 10.1130/G24207A.1)
- Joughin I and Alley RB (2011) Stability of the West Antarctic ice sheet in a warming world. *Nature Geosci.*, **4**(8), 506–513 (doi: 10.1038/ngeo1194)
- Joughin I and 7 others (1999) Tributaries of West Antarctic ice streams revealed by RADARSAT interferometry. *Science*, **286**(5438), 283–286 (doi: 10.1126/science.286.5438.283)
- Joughin I, Tulaczyk S, Bindschadler RA and Price S (2002) Changes in West Antarctic ice stream velocities: observation and analysis. *J. Geophys. Res.*, **107**(B11), 2289 (doi: 10.1029/2001JB001029)
- Joughin I and 6 others (2009) Basal conditions for Pine Island and Thwaites Glaciers, West Antarctica, determined using satellite and airborne data. *J. Glaciol.*, **55**(190), 245–257 (doi: 10.3189/002214309788608705)
- Karlsson NB, Rippin DM, Vaughan DG and Corr HFJ (2009) The internal layering of Pine Island Glacier, West Antarctica, from airborne radar-sounding data. *Ann. Glaciol.*, **50**(51), 141–146
- Lang O, Rabus BT and Dech SW (2004) Velocity map of the Thwaites Glacier catchment, West Antarctica. *J. Glaciol.*, **50**(168), 46–56 (doi: 10.3189/172756504781830268)
- Li X and 7 others (2010) Characterization of subglacial landscapes by a two-parameter roughness index. *J. Glaciol.*, **56**(199), 831–836 (doi: 10.3189/002214310794457326)
- MacGregor JA, Winebrenner DP, Conway H, Matsuoka K, Mayewski PA and Clow GD (2007) Modeling englacial radar attenuation at Siple Dome, West Antarctica, using ice chemistry and temperature data. *J. Geophys. Res.*, **112**(F3), F03008 (doi: 10.1029/2006JF000717)
- MacGregor J, Catania GA, Markowski MS and Andrews AG (2012a) Widespread rifting and retreat of ice-shelf margins in the eastern Amundsen Sea Embayment between 1972 and 2011. *J. Glaciol.*, **58**(209), 458–466 (doi: 10.3189/2012JoG11J262)
- MacGregor JA, Matsuoka K, Waddington ED, Winebrenner DP and Pattyn F (2012b) Spatial variation of englacial radar attenuation: modeling approach and application to the Vostok flowline. *J. Geophys. Res.*, **117**(F3), F03022 (doi: 10.1029/2011JF002327)
- Matsuoka K (2011) Pitfalls in radar diagnosis of ice-sheet bed conditions: lessons from englacial attenuation models. *Geophys. Res. Lett.*, **38**(5), L05505 (doi: 10.1029/2010GL046205)
- Nayar SK, Ikeuchi K and Kanade T (1991) Surface reflection: physical and geometrical perspectives. *IEEE Trans. Pattern Anal. Machine Intell.*, **13**(7), 611–634 (doi: 10.1109/34.85654)
- Ogilvy JA (1991) *Theory of wave scattering from random rough surfaces*. Institute of Physics Publishing, Bristol
- Oswald GKA and Gogineni SP (2008) Recovery of subglacial water extent from Greenland radar survey data. *J. Glaciol.*, **54**(184), 94–106 (doi: 10.3189/002214308784409107)
- Parizek BR and 10 others (2013) Dynamic (in)stability of Thwaites Glacier, West Antarctica. *J. Geophys. Res.*, **118** (doi: 10.1002/jgrf.20044)
- Peters ME, Blankenship DD and Morse DL (2005) Analysis techniques for coherent airborne radar sounding: application to West Antarctic ice streams. *J. Geophys. Res.*, **110**(B6), B06303 (doi: 10.1029/2004JB003222)
- Peters ME, Blankenship DD, Carter SP, Kempf SD, Young DA and Holt JW (2007) Along-track focusing of airborne radar sounding data from West Antarctica for improving basal reflection analysis and layer detection. *IEEE Trans. Geosci. Remote Sens.*, **45**(9), 2725–2736 (doi: 10.1109/TGRS.2007.897416)
- Pollard D and DeConto RM (2009) Modelling West Antarctic ice sheet growth and collapse through the past five million years. *Nature*, **458**(7236), 329–332 (doi: 10.1038/nature07809)
- Price SF, Bindschadler RA, Hulbe CL and Blankenship DD (2002) Force balance along an inland tributary and onset to Ice Stream D, West Antarctica. *J. Glaciol.*, **48**(160), 20–30 (doi: 10.3189/172756502781831539)
- Pritchard HD, Arthern RJ, Vaughan DG and Edwards LA (2009) Extensive dynamic thinning on the margins of the Greenland and Antarctic ice sheets. *Nature*, **461**(7266), 971–975 (doi: 10.1038/nature08471)
- Pritchard HD, Ligtenberg SRM, Fricker HA, Vaughan DG, Van den Broeke MR and Padman L (2012) Antarctic ice-sheet loss driven by basal melting of ice shelves. *Nature*, **484**(7395), 502–505 (doi: 10.1038/nature10968)
- Raymond C (1996) Shear margins in glaciers and ice sheets. *J. Glaciol.*, **42**(140), 90–102
- Raymond CF, Echelmeyer KA, Whillans IM and Doake CSM (2001) Ice stream shear margins. In Alley RB and Bindschadler RA eds. *The West Antarctic ice sheet: behavior and environment*. (Antarctic Research Series 77) American Geophysical Union, Washington, DC, 137–155
- Raymond CF, Catania GA, Nereson N and Van der Veen CJ (2006) Bed radar reflectivity across the north margin of Whillans Ice Stream, West Antarctica, and implications for margin processes. *J. Glaciol.*, **52**(176), 3–10 (doi: 10.3189/172756506781828890)
- Rignot E (2008) Changes in West Antarctic ice stream dynamics observed with ALOS PALSAR data. *Geophys. Res. Lett.*, **35**(12), L12505 (doi: 10.1029/2008GL033365)
- Rignot E and 11 others (2004) Improved estimation of the mass balance of the glaciers draining into the Amundsen Sea sector of West Antarctica from the CECS/NASA 2002 campaign. *Ann. Glaciol.*, **39**, 231–237 (doi: 10.3189/172756404781813916)
- Rignot E, Mouginot J and Scheuchl B (2011a) Ice flow of the Antarctic Ice Sheet. *Science*, **333**(6048), 1427–1430 (doi: 10.1126/science.1208336)
- Rignot E, Mouginot J and Scheuchl B (2011b) Antarctic grounding line mapping from differential satellite radar interferometry. *Geophys. Res. Lett.*, **38**(10), L10504 (doi: 10.1029/2011GL047109)
- Rippin DM, Bamber JL, Siegert MJ, Vaughan DG and Corr HFJ (2006) Basal conditions beneath enhanced-flow tributaries of Slessor Glacier, East Antarctica. *J. Glaciol.*, **52**(179), 481–490 (doi: 10.3189/172756506781828467)

- Rippin D, Vaughan DG and Corr HFJ (2011) The basal roughness of Pine Island Glacier, West Antarctica. *J. Glaciol.*, **57**(201), 67–76 (doi: 10.3189/002214311795306574)
- Ross N and 9 others (2012) Steep reverse bed slope at the grounding line of the Weddell Sea sector in West Antarctica. *Nature Geosci.*, **5**(6), 393–396 (doi: 10.1038/ngeo1468)
- Scambos TA, Bohlander JA, Shuman CA and Skvarca P (2004) Glacier acceleration and thinning after ice shelf collapse in the Larsen B embayment, Antarctica. *Geophys. Res. Lett.*, **31**(18), L18402 (doi: 10.1029/2004GL020670)
- Schoof C (2007) Ice sheet grounding line dynamics: steady states, stability, and hysteresis. *J. Geophys. Res.*, **112**(F3), F03S28 (doi: 10.1029/2006JF000664)
- Schroeder DM, Blankenship DD and Young DA (in press) Evidence for a water system transition beneath Thwaites Glacier, West Antarctica. *Proc. Natl Acad. Sci. USA (PNAS)* (doi: 10.1073/pnas.1302828110)
- Scott JBT, Gudmundsson GH, Smith AM, Bingham RG, Pritchard HD and Vaughan DG (2009) Increased rate of acceleration on Pine Island Glacier strongly coupled to changes in gravitational driving stress. *Cryosphere*, **3**(1), 125–131 (doi: 10.5194/tc-3-125-2009)
- Shepard MK, Campbell BA, Bulmer MH, Farr TG, Gaddis LR and Plaut JJ (2001) The roughness of natural terrain: a planetary and remote sensing perspective. *J. Geophys. Res.*, **106**(E12), 32 777–32 796 (doi: 10.1029/2000JE001429)
- Shepherd A, Wingham D and Mansley JA (2002) Inland thinning of the Amundsen Sea sector, West Antarctica. *Geophys. Res. Lett.*, **29**(10), 1364 (doi: 10.1029/2001GL014183)
- Shepherd A and 46 others (2012) A reconciled estimate of ice-sheet mass balance. *Science*, **338**(6111), 1183–1189 (doi: 10.1126/science.1227268)
- Smith AM and 6 others (2007) Rapid erosion, drumlin formation and changing hydrology beneath an Antarctic ice stream. *Geology*, **35**(2), 127–130 (doi: 10.1130/G23036A.1)
- Smith AM, Bentley CR, Bingham RG and Jordan TA (2012) Rapid subglacial erosion beneath Pine Island Glacier, West Antarctica. *Geophys. Res. Lett.*, **39**(12), L12501 (doi: 10.1029/2012GL051651)
- Stearns LA, Jezek KC and Van der Veen CJ (2005) Decadal-scale variations in ice flow along Whillans Ice Stream and its tributaries, West Antarctica. *J. Glaciol.*, **51**(172), 147–157 (doi: 10.3189/172756505781829610)
- Studinger M and 6 others (2001) Subglacial sediments: a regional geological template for ice flow in West Antarctica. *Geophys. Res. Lett.*, **28**(18), 3493–3496 (doi: 10.1029/2000GL011788)
- Ulaby FT, Moore RK and Fung AK (1982) *Microwave remote sensing, active and passive. Vol. 2. Radar remote sensing and surface scattering and emission theory*. Addison-Wesley, Reading, MA
- Van der Veen CJ (1999) *Fundamentals of glacier dynamics*. AA Balkema, Rotterdam
- Vaughan DG and 9 others (2006) New boundary conditions for the West Antarctic ice sheet: subglacial topography beneath Pine Island Glacier. *Geophys. Res. Lett.*, **33**(9), L09501 (doi: 10.1029/2005GL025588)
- Winsborrow MCM, Clark CD and Stokes CR (2010) What controls the location of ice streams? *Earth-Sci. Rev.*, **103**(1–2), 45–59 (doi: 10.1016/j.earscirev.2010.07.003)
- Young DA and 11 others (2011) A dynamic early East Antarctic Ice Sheet suggested by ice-covered fjord landscapes. *Nature*, **474**(7349), 72–75 (doi: 10.1038/nature10114)

APPENDIX: LATERAL SHEAR STRESS

The depth-averaged lateral shear stress is (e.g. Van der Veen, 1999; Price and others, 2002)

$$\bar{\tau}_{xy} = \bar{B} \dot{\epsilon}_e^{\frac{1}{n}} \dot{\epsilon}_{xy} \quad (\text{A1})$$

where \bar{B} is the depth-averaged temperature-dependent rate factor, $\dot{\epsilon}_e$ is the effective strain rate and n is the flow-law exponent (3). We estimate \bar{B} using the depth-averaged temperature derived from the original temperature model. The effective strain rate is

$$2\dot{\epsilon}_e^2 = \dot{\epsilon}_{xx}^2 + \dot{\epsilon}_{yy}^2 + \dot{\epsilon}_{zz}^2 + 2\dot{\epsilon}_{xy}^2 \quad (\text{A2})$$

We define x and y as the along-flow and across-flow directions, respectively; therefore, $\dot{\epsilon}_{yy}^2$ is explicitly zero. Following the incompressibility condition, $\dot{\epsilon}_{zz} = -\dot{\epsilon}_{xx} - \dot{\epsilon}_{yy}$, so the effective strain rate reduces to

$$\dot{\epsilon}_e = \sqrt{\dot{\epsilon}_{xx}^2 + \dot{\epsilon}_{xy}^2} \quad (\text{A3})$$

We calculate the horizontal strain rates $\dot{\epsilon}_{xx}$ and $\dot{\epsilon}_{xy}$ from gradients of the surface speed $|\bar{u}_s|$ projected onto the appropriate surface velocity unit vectors ($\hat{u}_{||}$ for x and \hat{u}_{\perp} for y) as

$$\dot{\epsilon}_{xx} = \frac{\partial u}{\partial x} = \bar{\nabla} |\bar{u}_s| \cdot \hat{u}_{||} \quad (\text{A4})$$

$$\dot{\epsilon}_{xy} = \frac{1}{2} \frac{\partial u}{\partial y} = \bar{\nabla} |\bar{u}_s| \cdot \hat{u}_{\perp} \quad (\text{A5})$$

Equation (A5) assumes that there are no longitudinal gradients in the lateral velocity v , i.e. $\partial v / \partial x = 0$.

MS received 15 March 2013 and accepted in revised form 14 June 2013